

Quasi-Static Continuum Model of Octopus-Like Soft Robot Arm Under Water Actuated by Twisted and Coiled Artificial Muscles (TCAMs)

Amirreza Fahim Golestaneh¹, Venanzio Cichella¹ and Caterina Lamuta¹

Abstract—The current work is a qualitative study that aims to explore the implementation of Twisted and Coiled Artificial Muscles (TCAMs) for actuating and replicating the bending motion of an octopus-like soft robot arm underwater. Additionally, it investigates the impact of hydrostatic and dynamic forces from steady-state fluid flow on the arm’s motion. The artificial muscles are lightweight and low-cost actuators that generate a high power-to-weight ratio, producing tensile force up to 12,600 times their own weight, which is close to the functionality of biological muscles. The “extended” Cosserat theory of rods is employed to formulate a quasi-static continuum model of arm motion, where the arm’s cross-section is not only capable of rigid rotation but also deforms within its plane. This planar deformation of the arm cross-section aligns with the biological behavior of the octopus arm, where the stiffness of the hydrostat is directly induced by the incompressibility of the tissues. In line with the main goal, a constitutive model is derived for the material of the octopus arm to capture its characteristic behavior.

Index Terms—Extended Cosserat Theory of Rods, Continuum Soft Robots, Twisted and Coiled Artificial Muscles (TCAMs), Octopus Arm Modeling, Fluid Flow Forces, Constitutive modeling.

I. INTRODUCTION

Early work on robot manipulation focused on discrete rigid manipulators, crafted to replicate the motion and grasping of the human hand [12]. These robots consist of rigid links connected by joints, culminating in an end-effector that interacts with the environment. Therefore, each degree of freedom (DOF) relies on an actuatable joint, which limits the system’s agility. Consequently, enhancing maneuverability requires adding more joints and DOFs, increasing complexity in both design and control. Besides *discrete* robots, Robinson et al. [31] categorized them into *serpentine* robots (also known as *hyper-redundant* manipulators) and *continuum* robots. Hyper-redundant manipulators typically feature a backbone structure with numerous actuatable joints, resulting in a DOF significantly greater than that of their operational workspace. For more details on modeling and solving the kinematics of hyper-redundant manipulators see early works [5]–[7]. They also employed the continuum formulation of kinematics to optimize the configuration of these manipulators [6]. A continuum robot is a type of manipulator that can locally change its configuration at any point along its length [40]. This allows it to navigate workspaces with obstacles and reach almost any point within them. Resembling the movements of snakes [24], elephant trunks [15], and octopus arms [21], continuum

robots theoretically possess infinite DOFs. However, unlike other manipulators, not every DOF is actuated, resulting in a relatively small number of actuators generating the motion [15]. These manipulators are typically actuated by cables, hydraulic, or pneumatic pressures [23], [29], [33].

The analysis of motion in continuum robots is categorized into piecewise constant-field techniques [8], [15], [17], [27], [35] and continuous-field techniques [3], [9], [26], [32], [39], [42]. One commonly adopted model for multi-sectional continuum robots is the piecewise constant curvature model, where it is assumed that the curvature remains constant along each section of the robot arm [8], [15], [17], [35]. The constant curvature technique becomes inaccurate in many scenarios, such as when significant external loads, like gravity, are present, or when there is considerable variation locally in the curvature of the robot arm [4], [37]. For more details on piecewise constant curvature model see [30].

The *standard* Cosserat theory of rods [1], widely adopted as a continuous-field technique, offers an accurate formulation for the motion of continuum robots [3], [9], [26], [32], [39], [42]. This approach utilizes strain fields corresponding to the rod’s deformation to derive the dynamic motion of the robot arm. Previous works [10], [27] explains how standard Cosserat theory is implemented to model a cable-driven soft robot arm, followed by the application of the piecewise constant-strain technique for discretization [27]. This approach was further developed in [26] to incorporate a variable-strain methodology. Similarly, in [3], a strain-based technique was employed to construct a nonlinear parametrization of the Cosserat model for the soft robot arm and to conduct dynamic motion analysis. Unlike the standard Cosserat theory, which focuses solely on the deformation of the entire rod, the *extended Cosserat* theory of rods also incorporates planar deformation within the rod’s cross-section alongside the rod’s overall deformation [19]. This implies that, the cross-section of the rod can undergo both rigid rotation and deformation within its plane. Incorporating the deformation in rod cross section can inherently enhance the dynamic analysis of the robot arm motion particularly for arms that undergo substantial deformations. For more details on application of Cosserat rod theory in modeling of continuum robots, see reviews [2], [25].

The recently developed Twisted and Coiled Artificial Muscles (TCAMs) offer lightweight and cost-effective alternatives to traditional actuators, such as electromagnetic motors, and hydraulic and pneumatic actuators [22], [38], [43]. These artificial muscles generate a high power-to-weight ratio, producing

¹ The authors are with the Department of Mechanical Engineering, University of Iowa, Iowa City, IA 52240 {amirreza-fahimgolestaneh, venanzio-cichella, caterina-lamuta}@uiowa.edu

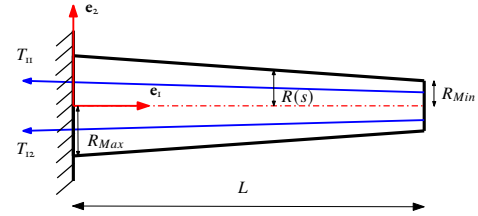
tensile forces up to 12,600 times their own weight, closely resembling the functionality of biological muscles [18], [34]. The integration of TCAM actuators in soft robotics is rapidly growing due to their high power-to-weight ratio and low manufacturing cost [34]. This application necessitates a thorough understanding and the development of a theoretical dynamic model of TCAMs to accurately describe their actuation behavior and facilitate the design of control algorithms. As discussed in [41], TCAM dynamics are categorized into fitting-based models, which derive constant parameters from experimental data, and physics-based models, utilizing constitutive relations. Weerakkody et al. [41] developed a physics-based model akin to Giovinco et al. [11] for TCAM actuation, introducing an adaptive control algorithm. This model extends their earlier static work in [20], comprising a thermal model linking input voltage or heat to fiber radius expansion in TCAMs, and a mechanical model describing how this radius expansion relates to generated tensile force in TCAMs. For more details on physics-based modeling of artificial muscles, refer to [11], [14], [20], [36].

The primary goal of this work is to study the impact of hydrostatic and dynamic forces from steady-state fluid flow on the motion of a robot arm driven by TCAMs. Throughout this paper, the extended Cosserat theory of rods models an octopus-like soft robot arm as a continuum robot, allowing for both rigid rotation and planar deformation of the rod's cross-section. This implies that the cross-section is not locally constrained to be perpendicular to the rod's direction at any point along its length, which is crucial for modeling hollow rods and those with significant bending deformations, such as octopus arms. The planar deformation of the cross-section is aligned with the biological behavior of octopus arms, where the stiffness of the hydrostat is induced by tissue incompressibility. The study explores the application of recently developed electro-thermo TCAMs, developed by some of the authors, to actuate and replicate the motion of octopus arms. A physics-based dynamic model of TCAMs is discussed to characterize their time-varying tensile actuation. Furthermore, a constitutive model is derived for the material of the octopus arm to capture its characteristic behavior.

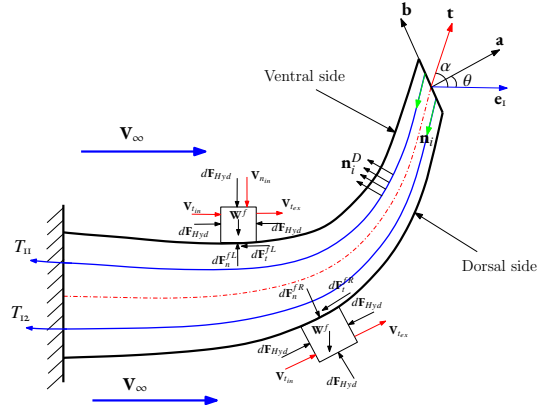
II. EXTENDED COSSERAT THEORY OF RODS

A. Configuration of Rod

Fig. 1 shows both the reference (undeformed) straight configuration and the deformed configuration of the octopus-like arm, actuated by two longitudinal TCAMs. The *extended* Cosserat theory of rods [19] is used to model the configuration of the robot arm. This theory retains the standard Cosserat framework, including all strains and governing equations that describe the bulk rod deformation, while adding new strains with corresponding equations to account for cross-sectional deformation. For a two-dimensional (2D) rod, this involves introducing a new normal strain $\beta \in \mathbb{R}$ to represent the planar deformation of the cross section, followed by the rigid rotation $\mathbf{R} \in \mathbb{SO}(2)$ to determine the orientation of the cross section. The configuration of the robot arm, $\mathbf{x} : [0, L] \mapsto \mathbb{R}^2$, is



(a) Reference (undeformed) straight arm.



(b) Deformed arm.

Fig. 1: Octopus arm actuated by two TCAMs.

parametrized by the curve length $s \in [0, L]$ of the centerline of the undeformed straight rod:

$$\mathbf{x}(s) = \mathbf{r}(s) + x_2(X_2(s), s)\mathbf{b}(s), \quad (1)$$

where $\mathbf{r}(s)$ represents the centerline of the rod, $x_2(X_2(s), s) \doteq \beta(s)X_2(s)$ such that $|X_2(s)|$ is the radius of undeformed rod and $\beta(s) = \frac{\partial x_2(s)}{\partial X_2(s)}$ accounts for the planar deformation of the cross section along \mathbf{b} . The standard orthonormal *directors* $\mathbf{a}(s) = \cos(\theta)\mathbf{e}_1 + \sin(\theta)\mathbf{e}_2$ and $\mathbf{b}(s) = -\sin(\theta)\mathbf{e}_1 + \cos(\theta)\mathbf{e}_2$ determine the rotation matrix $\mathbf{R} = [\mathbf{a} \ \mathbf{b}]$, where $\{\mathbf{e}_1, \mathbf{e}_2, \mathbf{k}\}$ form the global fixed Cartesian frame located on the centerline at $s = 0$ and angle $\theta(s) : [0, L] \mapsto \mathbb{R}$ defines the orientation of \mathbf{a} (see Fig. 1b).

B. Bulk Strains

In standard Cosserat theory of rods, the bulk translational strains, which correspond to the deformation of the entire rod, are defined as the components of $\mathbf{r}_s \in \mathbb{R}^2$ represented in the standard body frame $\{\mathbf{a}, \mathbf{b}\}$

$$\mathbf{t}(s) \doteq \mathbf{r}_s(s) = \nu(s)\mathbf{a}(s) + \eta(s)\mathbf{b}(s), \quad (2)$$

where $\nu \in \mathbb{R}$ and $\eta \in \mathbb{R}$ respectively measure the normal and shear translational bulk strains and subscript s signifies spatial derivative $(\)_s \doteq \partial_s(\)$. Similarly, the bulk bending strains are defined as the components of \mathbf{a}_s and \mathbf{b}_s , expressed in the standard body frame:

$$\begin{aligned} \mathbf{a}_s(s) &= R_s(s)\mathbf{e}_1 = \mu\mathbf{b}, \\ \mathbf{b}_s(s) &= R_s(s)\mathbf{e}_2 = -\mu\mathbf{a}, \end{aligned} \quad (3)$$

where the bending strain $\mu(s) = \partial_s \theta(s) \in \mathbb{R}$ locally measures the curvature of the centerline. The skew-symmetric matrix $\xi(s) \doteq \mathbf{g}^{-1} \mathbf{g}_s = \begin{bmatrix} \mathbf{R}^T \mathbf{R}_s & \mathbf{R}^T \mathbf{r}_s \\ 0 & 0 \end{bmatrix} \in \mathfrak{se}(2)$ captures the bulk strains, where $\mathbf{g}(s) \doteq \begin{bmatrix} \mathbf{R} & \mathbf{r} \\ 0 & 1 \end{bmatrix} \in \mathbb{SE}(2)$ is the rigid body transformation. The centerline \mathbf{r} is calculated from strains by:

$$\begin{aligned} r_s^a(s) &= \nu + \mu r^b, \\ r_s^b(s) &= \eta - \mu r^a, \end{aligned} \quad (4)$$

where r^a and r^b are its coordinates in standard body frame.

III. TCAMS ACTUATION MODEL

This section reviews the theory behind the recently developed electro-thermo TCAMs, by some of the authors [41]. The theory consists of a thermal model and a mechanical model, which together describe the time-varying tensile actuation of TCAMs. The thermal model details the relationship between the input voltage or heat and the increase in the fiber radius in electro-thermally actuated TCAMs. The mechanical model relates the increase in fiber radius to the generated tensile force in the TCAMs.

A. Thermal Model For TCAMs

TCAMs are manufactured by coating fibers with a thermally active polymer, then twisting them until they spontaneously coil. They undergo precise heat treatment to enable contraction when activated by electro-thermal stimuli. This contraction is caused by anisotropic volume expansion of the TCAM fibers after stimulation. The fibers' anisotropic thermal properties cause their radius to increase upon exposure to heat, Joule heating, or absorption of a chemical solvent, while maintaining a constant length. For some materials like nylons, the fiber length shortens while the radius increases after stimulation [13]. The increase in fiber radius $r_{tm} \in \mathbb{R}^+$ can be linearly correlated with the rise in temperature:

$$\frac{r_{tm}(\bar{T}_\Delta) - r_{tm}^o}{r_{tm}^o} = \alpha \bar{T}_\Delta(t), \quad (5)$$

where $\alpha \in \mathbb{R}^+$ is the linear thermal expansion coefficient in the radial direction, $r_{tm}^o \in \mathbb{R}^+$ denotes the initial fiber radius and $\bar{T}_\Delta = \bar{T}(t) - \bar{T}_{amb} \in \mathbb{R}$ is the change in temperature such that $\bar{T}_{amb} \in \mathbb{R}^+$ represents the ambient temperature. When the TCAMs are electro-thermally stimulated, the relationship between the input voltage $v_{vol}(t) \in \mathbb{R}$ and the change in temperature $\bar{T}_\Delta \in \mathbb{R}$ can be defined by [44]:

$$\dot{\bar{T}}_\Delta(t) = \frac{v_{vol}^2(t)}{C_t R_{vol}} - \frac{\lambda(\bar{T}_\Delta)}{C_t} \bar{T}_\Delta, \quad (6)$$

where $\dot{(\cdot)}$ represents time derivative and $C_t = mc_p \in \mathbb{R}^+$, $R_{vol} \in \mathbb{R}^+$ and $\gamma = hA_s \in \mathbb{R}^+$ are respectively the thermal mass, electrical resistance, and the absolute thermal conductivity of the TCAM. Here, $m \in \mathbb{R}^+$ is the mass of the TCAM, $A_s \in \mathbb{R}^+$ is its cross section, $h \in \mathbb{R}^+$ is the convection coefficient between the actuator and the environment, and $c_p \in \mathbb{R}^+$ is the TCAM specific heat.

B. Mechanical Model For TCAMs

The increase in the radius of TCAM fibers and the consequent anisotropic volume expansion of the fibers stiffen the bending and torsional deformations of the TCAMs, such that:

$$\begin{aligned} B(\bar{T}_\Delta) &= E_x \frac{\pi}{4} r_{tm}^4(\bar{T}_\Delta), \\ C(\bar{T}_\Delta) &= G_{yz} \frac{\pi}{2} r_{tm}^4(\bar{T}_\Delta), \end{aligned} \quad (7)$$

where $E_x, G_{yz} \in \mathbb{R}^+$ are respectively normal Young's modulus and shear modulus of TCAMs. The variation in bending and torsion stiffness of the TCAMs causes the change in the TCAMs geometry of coil angle $\beta(\bar{T}_\Delta) \in \mathbb{R}$

$$\cos(\beta(\bar{T}_\Delta)) = 1 - \frac{\left(\frac{qB(\bar{T}_\Delta)C(\bar{T}_\Delta)}{\sqrt{B(\bar{T}_\Delta)\bar{m}g^r} - 2C(\bar{T}_\Delta)} \right)}{B(\bar{T}_\Delta) - C(\bar{T}_\Delta)}, \quad (8)$$

where $q = \frac{2\pi n}{S} \in \mathbb{R}^+$ denotes the total end rotation of the fiber, $n \in \mathbb{R}^+$ is the number of turns and $\bar{m} \in \mathbb{R}^+$ denotes the external mass applied to the end of the TCAMs during the coiling process (the TCAM mass is neglected compared to mass \bar{m}). Here, $g^r \in \mathbb{R}^+$ is the magnitude of gravity acceleration. The length of the TCAM after contraction is then calculated as:

$$\mathcal{L}(t) = \bar{S} \cos(\beta(\bar{T}_\Delta)). \quad (9)$$

The dynamics of TCAMs actuation is modeled as a second-order mass-spring-damper system, governed by:

$$m\ddot{\mathcal{L}}(t) + b(\bar{T}_\Delta(t))\dot{\mathcal{L}}(t) + k(\bar{T}_\Delta(t))\mathcal{L}(t) = F_e(t), \quad (10)$$

where $b(\bar{T}_\Delta(t)) \in \mathbb{R}^+$ and $k(\bar{T}_\Delta(t)) \in \mathbb{R}^+$ and $F_e(t) \in \mathbb{R}$ are respectively the time-dependent damping coefficient, the spring coefficient of the TCAMs and the external force applied to the system. Considering an equilibrium configuration such that $F_e(t) = \bar{m}g$, where $\dot{\mathcal{L}}(t) = \dot{\mathcal{L}}(t) = 0$, then the time-dependent spring coefficient of the TCAMs is obtained:

$$k(\bar{T}_\Delta) = \frac{\bar{m}g}{\bar{S} \cos(\beta(\bar{T}_\Delta))}. \quad (11)$$

The time-dependent damping coefficient $b(\bar{T}_\Delta) \in \mathbb{R}^+$ of the TCAMs is calculated in correspondence to the viscosity coefficient $\eta(\bar{T}_\Delta) \in \mathbb{R}^+$ of the TCAMs, where the Kelvin-Voigt viscoelastic theory is used to describe the constitutive behavior of the TCAMs as a viscoelastic material [16]

$$b(\bar{T}_\Delta) = \frac{\eta(\bar{T}_\Delta)A_s}{\bar{\mathcal{L}}}. \quad (12)$$

Now let define the TCAMs contraction as $d(t) = \mathcal{L}_o - \mathcal{L}(t)$, where the initial length of the TCAMs $\mathcal{L}_o > 0$ at time $t = 0$ for ambient temperature of TCAMs $\bar{T}(t=0) = \bar{T}_{amb}$ is calculated as $\mathcal{L}_o = \frac{\bar{m}g}{k_o}$, where $k_o \doteq k(\bar{T}_\Delta(t=0) = 0)$. The dynamic equation of motion of TCAMs (10) is reformulated:

$$\begin{aligned} m\ddot{d}(t) + b(\bar{T}_\Delta(t))\dot{d}(t) + k_o d(t) = \\ k(\bar{T}_\Delta(t))\mathcal{L}_o - F_e - k_\Delta(t)d(t), \end{aligned} \quad (13)$$

where $k_\Delta(t) \doteq k(\bar{T}_\Delta(t)) - k_o$. Linearize (13) by considering $C\bar{T}_\Delta(t) \approx k(\bar{T}_\Delta(t))\mathcal{L}_o - F_e - k_\Delta(t)d(t)$, where the coefficient

C can be experimentally approximated by some arbitrary constant temperature \bar{T}_Δ^* . Consider the equilibrium condition from (13) at an arbitrary time $t^* > 0$ with arbitrary temperature \bar{T}^* and $\bar{T}_\Delta^*(t^*) = \bar{T}^*(t^*) - \bar{T}_{amb}$, where $\dot{L}(t^*) = \dot{L}(t^*) = 0$:

$$k_o d^*(t^*) \approx CT_\Delta^*(t^*), \quad (14)$$

where $d^*(t^*) = \mathcal{L}_o - \frac{mg}{k(\bar{T}_\Delta^*(t^*))}$ such that $k(\bar{T}_\Delta^*(t^*))$ is calculated from (11). Therefore, the coefficient C is:

$$C = \frac{k_o d^*(t^*)}{\bar{T}_\Delta^*(t^*)} \quad (15)$$

and the dynamic equation of motion of the TCAMs is approximated as:

$$m\ddot{d}(t) + b(\bar{T}_\Delta(t))\dot{d}(t) + k_o d(t) \approx \frac{k_o d^*(t^*)}{\bar{T}_\Delta^*(t^*)} \bar{T}_\Delta(t), \quad (16)$$

where $\bar{T}_\Delta(t)$ is associated to the applied input voltage $V(t) \in \mathbb{R}^+$ through the ODE in (6).

IV. EXTERNAL AND INTERNAL LOADS

A. Concentrated Force of TCAMs

The concentrated force $\mathbf{f}_{ij}^{cc}(L_i) \in \mathbb{R}^2$ of the TCAMs $j \in \{1, 2\}$ of the segment $i \in \mathbb{Z}^+$ is modeled as [28]:

$$\mathbf{f}_{ij}^{cc}(L_i) = -T_{ij} \mathbf{t}_{ij}^c(L_i), \quad (17)$$

where $L_i \in (0, L]$ is the length of undeformed centerline of the segment $i \in \mathbb{Z}^+$ and $T_{ij} \in \mathbb{R}^+$ denotes the tension of the corresponding TCAMs and segment

$$T_{ij}(\bar{t}) = \frac{k_o d^*(t^*)}{\bar{T}_\Delta^*(t^*)} \bar{T}_\Delta^{ij}(\bar{t}). \quad (18)$$

In this context, the segment refers to an individual, flexible section of the arm that is actuated independently, allowing fine control over complex shapes. The temperature $\bar{T}_\Delta^{ij}(\bar{t})$ at any fixed time $\bar{t} \in \mathbb{R}^+$ is associated to the applied input voltage $V^{ij}(\bar{t}) \in \mathbb{R}^+$ through the ODE in (6). The $\mathbf{t}_{ij}^c(s) = \frac{\partial \mathbf{r}_{ij}^c(s)}{\partial s}$ for $s \in [0, L_i]$ is the tangent vector to the TCAMs, such that the position vector $\mathbf{r}_{ij}^c(s) \in \mathbb{R}^2$ of the TCAMs $j \in \{1, 2\}$ of the segment $i \in \mathbb{Z}^+$ is determined by $\mathbf{r}_{ij}^c(s) = \mathbf{r}(s) + y_{ij}^c(s)\beta(s)\mathbf{b}(s)$, where $y_{ij}^c(s) \in \mathbb{R}$ denotes the distance of that TCAMs from the undeformed centerline.

B. Distributed Force of TCAMs

The distributed force per unit length $\mathbf{f}_{ij}^{cd}(s) \in \mathbb{R}^2$ of the TCAMs $j \in \{1, 2\}$ along the undeformed centerline $s \in [0, L_i]$ of segment $i \in \mathbb{Z}^+$ is modeled as [28]:

$$\mathbf{f}_{ij}^{cd}(s) = T_{ij} \frac{\partial \mathbf{t}_{ij}^c(s)}{\partial s}. \quad (19)$$

Therefore, the moment $\mathbf{m}_{ij}^{cd}(s) \in \mathbb{R}^2$ about the origin of the fixed global Cartesian frame is:

$$\mathbf{m}_{ij}^{cd}(s) = \int_s^{L_i} \mathbf{r}_{ij}^c(\delta) \times T_{ij} \frac{\partial \mathbf{t}_{ij}^c(\delta)}{\partial \delta} d\delta. \quad (20)$$

C. Fluid Forces

The primary objective is to investigate how hydrostatic and dynamic forces from a steady-state fluid flow affect the bending motion of an octopus-like robot arm propelled by TCAMs. The study focuses on analyzing the static deformation of the arm as the tension in the TCAMs incrementally increases. To achieve this goal, a viscous fluid flow with a quadratic velocity profile $\mathbf{v}_t(s, y)$ is introduced over the arm. This velocity profile varies with the normal distance $y \in [0, h_\infty]$ from the arm's surface, satisfying the no-slip condition on the arm's surface. The velocity monotonically increases to its maximum v_{t_∞} at a distance h_∞ from the arm's surface

$$\mathbf{v}_t(s, y) = v_{t_\infty}(s) \left[\frac{2y}{h_\infty} - \left(\frac{y}{h_\infty} \right)^2 \right] \mathbf{u}_t(s). \quad (21)$$

The subscript t signifies the tangential direction to the surface of the arm such that $\mathbf{u}_t(s) = \frac{\partial_s \mathbf{x}(s)}{\|\partial_s \mathbf{x}(s)\|}$ is the tangent unit vector to the arm surface and $v_{t_\infty}(s) = \mathbf{v}_\infty \cdot \mathbf{u}_t(s)$ is the tangential component of the free-stream velocity $\mathbf{v}_\infty = v_\infty \mathbf{e}_1$ of the fluid flow. The quadratic velocity profile \mathbf{v}_t in (21) is used to calculate the viscous frictional force $d\mathbf{F}_{vis}(s) \in \mathbb{R}^2$ applied to the infinitesimal surface of the arm opposite to the direction of the flow:

$$d\mathbf{F}_{vis}(s) = \frac{-2\pi X_2(s)\beta\mu_v v_{t_\infty}(s)}{h_\infty} \mathbf{u}_t(s) ds, \quad (22)$$

where μ_v is the dynamic viscosity of the fluid. The continuity equation and the principle of linear momentum for a steady state flow is applied separately over two infinitesimal control volumes of fluid on ventral and dorsal surfaces of the arm to compute the tangential $d\mathbf{F}_t^V(s)$ and normal $d\mathbf{F}_n^V(s)$, $d\mathbf{F}_n^D(s)$ hydrostatic and dynamic contact forces applied by the fluid to the ventral and dorsal infinitesimal surfaces of the arm:

$$d\mathbf{F}_t^V(s) = (v_{n_{in}}^2(s) + 2v_{t_{in}}(s)v_{n_{in}}(s)) \pi \rho_w \beta X_2 ds \mathbf{u}_t(s), \quad (23)$$

$$d\mathbf{F}_n^V(s) = [d\mathbf{F}_{Hyd}(s) + \pi \rho_w \beta X_2 v_{n_{in}}^2(s) ds] \mathbf{u}_n(s), \quad (24)$$

$$d\mathbf{F}_n^D(s) = d\mathbf{F}_{Hyd}(s) \mathbf{u}_n(s). \quad (25)$$

$\mathbf{F}_{Hyd}(s)$ denotes the hydrostatic force of fluid, $\rho_w \in \mathbb{R}^+$ is the density of fluid, the superscripts V and D respectively signify the ventral and dorsal surfaces of the arm, subscript n signifies the normal direction to the surface of the arm and subscript in signifies the inlet open surface of the control volume and its corresponding quantities. The weight of the infinitesimal control volume of the fluid is negligible compared to the other existing forces and therefore it is ignored in these computations. The normal component $v_n(s)$ of the free-stream velocity $\mathbf{v}_\infty = v_\infty \mathbf{e}_1$ is $v_n(s) = \mathbf{v}_\infty \cdot \mathbf{u}_n(s)$, where $\mathbf{u}_n(s) = \mathbf{k} \times \mathbf{u}_t(s)$ such that $\|\mathbf{k} \times \mathbf{u}_t(s)\| = 1$ and $\{\mathbf{u}_t, \mathbf{u}_n, \mathbf{k}\}$ forms an orthonormal local body frame of reference.

The inlets and outlets of the control volume are determined in accordance with the direction of the velocity of the flow at each open surface of the control volume. The left and top surfaces of the control volume on the ventral surface of the arm serve as inlets, while the right surface is an outlet. Similarly,

the left and right surfaces of the control volume on the dorsal surface of the arm are, respectively, an inlet and an outlet, with the flow through the top surface assumed to be negligible (see Figure 1b).

It is notable that the resultant normal force $d\mathbf{F}_n^V$ in (24), applied to the infinitesimal ventral surface of the arm, comprises both the hydrostatic force of the fluid and the dynamic force generated by the change in velocity (linear momentum) of the fluid flow between the inlet and outlet of the control volume from $\mathbf{v}_{n_{in}}$ to 0. The resultant normal force $d\mathbf{F}_n^D$ in (25), applied to the infinitesimal dorsal surface of the arm, comprises only the hydrostatic force of the fluid, as the fluid flow through the top surface of the control volume is assumed negligible. The resultant tangential force $d\mathbf{F}_t^V$ in (23), applied to the infinitesimal ventral surface of the arm, consists of the force generated by the change in velocity (linear momentum) of the fluid flow between the inlet and outlet of the control volume from $\mathbf{v}_{t_{in}}$ to $\mathbf{v}_{t_{in}} + \mathbf{v}_{n_{in}}$. This indicates that the fluid flow exerts both hydrostatic and dynamic resultant forces on the surface of the arm, influencing the configuration of the deformed arm underwater.

D. Weight of Segment of Arm

In the deformed configuration of the arm, the cross section is oriented along \mathbf{b} , and \mathbf{a} is not necessarily tangent to the centerline. Therefore, the weight of a segment of the deformed arm between $\delta \in [s, L]$ is calculated as:

$$\mathbf{W}(s) = -\pi\rho g^r \int_{\delta=s}^L \nu(\delta) \{\beta(\delta)X_2(\delta)\}^2 d\delta \mathbf{e}_2, \quad (26)$$

where $\rho \in \mathbb{R}^+$ denotes the density of the arm material. The normal strain ν appears in (26) to align the rod's cross section with the direction of its centerline.

E. Resultant Contact Force and Moment

The constitutive model of the soft robot material connects the strains to the internal contact forces and moments. Since the contact force is not always aligned with the normal unit director \mathbf{a} of the deformed cross section, it is expressed in the local standard body frame:

$$\mathbf{f}^c(s) \doteq \{N(s)\mathbf{a}(s) + H(s)\mathbf{b}(s)\} A(s), \quad (27)$$

where $A(s) = \pi(\beta(s)X_2(s))^2$, and N and H represent the normal and shear forces per unit area (tractions) of the cross section, which correspond to the normal and shear strains ν and η , respectively. The constitutive model of the arm material defines the resultant contact moment in the local standard body frame as:

$$\mathbf{m}^c(s) \doteq M(s)J_k(s)\mathbf{k}, \quad (28)$$

where M is proportional to the magnitude of the bending moment and corresponds to the bending strain (local curvature) μ . $J_k(s) = \frac{\pi(\beta X_2)^4}{4} \in \mathbb{R}$ is the second moment of inertia of the circular cross section of the rod about \mathbf{k} axis.

V. CONSTITUTIVE MODEL

The behavior of the soft material of the robot arm is described by a hyperelastic model. In a hyperelastic material, the stress field is a conservative function derived from a scalar-valued function called the strain energy function, by taking its derivative with respect to the strain field. Let's assume the strain energy function ψ for the robot arm is a quadratic polynomial of bulk strains:

$$\psi(\nu, \eta, \mu, s) = C_1(s)(\nu - \nu_o)^2 + C_2(s)(\eta - \eta_o)^2 + C_3(s)(\mu - \mu_o)^2, \quad (29)$$

where $C_1(s)$, $C_2(s)$ and $C_3(s)$ respectively denote the normal, shear and bending stiffness coefficients of the arm material. The constitutive equations for a continuum material must meet specific criteria to accurately model its behavior. The strain energy function needs to be sufficiently smooth as the quadratic polynomial in (29) is infinitely continuously differentiable $\psi(\nu, \eta, \mu, s) \in C^\infty(\mathbb{R}^3)$, assuming $\nu, \eta, \mu, C_i(s) \in C^\infty(\mathbb{R})$ for $i \in 1, 2, 3$. In this work, the reference (straight) configuration of the rod is defined as an undeformed configuration where all bulk and cross-sectional strains vanish. It is also intended that the natural (stress-free) configuration coincides with the reference configuration, ensuring the strain energy function is minimized, thereby causing stress to vanish. Consequently, the straight reference configuration aligns with both the undeformed and stress-free configurations, resulting in vanishing strains and stresses. The tractions $N(s), H(s), M(s) \in \mathbb{R}$ are required to monotonically increase. This implies that any increase in bulk strains $\nu(s), \eta(s)$, and $\mu(s)$ induces an increase in the corresponding tractions $N(s), H(s)$, and $M(s)$, such that each traction reaches its maximum at the maximum of the respective bulk strain. The following constitutive equations are proposed here for these tractions based on the necessary conditions required for the strain energy function ψ

$$\begin{aligned} N(s) &= \frac{\partial \psi}{\partial \nu} = 2C_1(\nu(s) - 1), \\ H(s) &= \frac{\partial \psi}{\partial \eta} = 2C_2\eta(s), \\ M(s) &= \frac{\partial \psi}{\partial \mu} = 2C_3\mu(s), \end{aligned} \quad (30)$$

where $C_1 = C_3 = E \in \mathbb{R}^+$ and $C_2 = G \in \mathbb{R}^+$. The Young modulus E and for an isotropic material the shear modulus G are related by $G = \frac{E}{2(1+\nu_p)}$, where $\nu_p \in [0, 0.5]$ is the Poisson's ratio. It is notable that since $N(s), H(s)$ and $M(s)$ in (30) monotonically increase, they are injective and invertible functions. This implies the existence of conjugate constitutive fields $\nu(N, H, M, s), \eta(N, H, M, s)$ and $\mu(N, H, M, s)$.

VI. GOVERNING EQUATIONS FOR BULK STRAINS

To derive the governing equations for the system, the translational and rotational equations of equilibrium are utilized in their local forms. This results in three scalar-valued governing equations for the bulk strains ν, η , and μ . These equations are formulated as a system of three nonlinear ordinary differential

equations (ODEs). The vector form of the governing equations is expressed as follows:

$$\mathbf{f}_s^c(s) + \mathbf{f}^{cd} + \mathbf{f}^{ex}(s) + \mathbf{w}(s) = \mathbf{0}, \quad (31)$$

$$\mathbf{m}_s^c(s) + (\mathbf{r}(s) \times \mathbf{f}^c(s))_s + \mathbf{m}_s^{cd} + \mathbf{m}^{ex}(s) + \mathbf{m}_s^w = \mathbf{0}, \quad (32)$$

where $\mathbf{f}^{ex} \doteq d\mathbf{F}_{vis} + d\mathbf{F}_t^V + d\mathbf{F}_n^V + d\mathbf{F}_n^D$ using (19), (22), (23), (24), (25) and (27). Here, \mathbf{w} is the weight of the arm per unit length of straight centerline, which is obtained from (26). For (32) use (20) and (28), where $\mathbf{m}^{ex} \doteq \mathbf{x} \times \mathbf{f}^{ex}$ and \mathbf{m}^w denotes the moment of the arm's weight in (26) about the origin of the fixed global Cartesian frame.

VII. LOCAL VOLUME PRESERVATION CONSTRAINT

The constraint of local volume preservation aligns with the biological characteristics of muscular hydrostats such as octopus arms. In these structures, tissue incompressibility directly influences the stiffness of the hydrostat. Therefore, the deformation of the octopus arm is constrained by:

$$\frac{\partial v(s)}{\partial V(s)} = \det(F(s)) = 1, \quad (33)$$

where V and v are respectively the volumes of undeformed and deformed robot arms and $F(s) \in \mathbb{R}^{2 \times 2}$ denotes the deformation gradient tensor:

$$F(s) \doteq \frac{\partial \mathbf{x}(s)}{\partial \mathbf{X}(s)} = \frac{\partial \mathbf{x}(s)}{\partial X_\alpha(s)} \otimes \mathbf{e}_\alpha, \quad (34)$$

where $\mathbf{X}(s) = s \mathbf{e}_1 + X_2(s) \mathbf{e}_2$ describes the straight arm, $X_1 \equiv s$ and $X_2 \equiv X_2(s)$ for $\alpha \in \{1, 2\}$ and \otimes denotes the tensor product of two vectors. The local volume preservation constraint in (33) introduces a governing equation for the new cross-sectional normal strain $\beta \in \mathbb{R}$:

$$\beta_s(s) = \frac{-\beta(\nu_s - \beta \partial_s X_2 \mu - \beta X_2 \mu_s)}{\nu - 2\beta X_2 \mu}. \quad (35)$$

Note that the local volume preservation constraint in (33) is satisfied only by the strain β in (35), without any corresponding internal force or moment associated with β . This contrasts with scenarios where the local volume preservation constraint is enforced on the strain energy function using a Lagrange multiplier, such as pressure (stress). In that case, there is no strain directly conjugate to the pressure, meaning the pressure is not computed through a constitutive equation.

VIII. RESULTS AND DISCUSSIONS

In this section, we apply the previously discussed general formulations to a specific case study. This case study focuses on an octopus-like soft robot arm with a straight undeformed configuration and a truncated conic geometry that is characterized by a radius of $|X_2(s)|$ [28]

$$|X_2(s)| = \left(\frac{R_{min} - R_{max}}{L} \right) s + R_{max} \quad (36)$$

such that $R_{max} \geq R_{min} > 0$ denote the maximum and minimum radii of the undeformed rod cross sections, respectively.

The distance $y_{ij}^c(s) \in \mathbb{R}$ of the TCAMs $j \in \{1, 2\}$ in segment $i \in \mathbb{Z}^+$ from the undeformed centerline is calculated as:

$$y_{ij}^c(s) = (-1)^{(j-1)} \left\{ \left(\frac{b_i - a_i}{L_i} \right) s + a_i \right\}, \quad (37)$$

where $0 < b_i < a_i$ such that $a_i \in \mathbb{R}^+$ and $b_i \in \mathbb{R}^+$ represent the distances of each TCAM in segment $i \in \mathbb{Z}^+$ from the undeformed centerline of the rod successively at the beginning and end of that segment. In this setup, electro-thermo carbon fibers/silicone rubber TCAMs are employed to actuate the octopus robot arm. These TCAMs are driven by a sinusoidal input voltage $v_{vol}(t) = V_{amp} \sin(\omega_{vol} t)$, where $V_{amp} = 9$ V is the amplitude and $\omega_{vol} = 1$ rad/sec is the angular frequency. Table I tabulates the parameters of these TCAMs [14].

TABLE I: Parameters of TCAMs.

Parameters	Values
m	0.106 Kg
\bar{m}	0.106 Kg
\bar{S}	0.46 m
\bar{L}_{amb}	0.418 m
n	200
r_{lm}^o	3.6×10^{-4} m
T_{amb}	23 °C
C_{TE}	3×10^{-4} C ⁻¹
C_t	0.162 JC ⁻¹
R_{vol}	18 Ω
E_x	4.67×10^8 Pa
G_{yz}	2.2×10^7 Pa
λ	0.0086 WC ⁻¹

1) *Results:* Fig. 2a shows that the temperature of the electro-thermo TCAMs, stimulated by the sinusoidal voltage, rises to 98, °C. Correspondingly, the TCAMs' tensile force in Fig. 2b increases similarly, reaching 25 N. It is important to note that the functionality of the TCAMs is highly dependent on temperature, with potential malfunctions occurring beyond a certain threshold. Fig. 2a indicates that the TCAMs are operating within a feasible temperature range. The system of four coupled nonlinear ODEs (31), (32) and (35) forms a quasi-static model. This model is used to study the effects of hydrostatic and dynamic forces from steady-state fluid flow on the bending motion of an octopus-like robot arm driven by TCAMs. The deformed configuration of the arm is analyzed statically at each incremental increase in the tension of the TCAMs. The model is numerically solved for the four unknown strain fields: normal strain ν , shear strain η , bending strain μ , and cross-sectional normal strain β , under the boundary conditions (BCs) for the fixed support arm: $\nu_o = \beta_o = 1$ and $\eta_o = \mu_o = \beta'_o = 0$. In this section, the application of the model to two case studies involving free-stream velocities $v_\infty = 0.2$ m/s and 0.4 m/s of steady-state water flow is presented. For each case study, a step size of 0.5 N is used to incrementally increase the tension $T_{11} \in [0, 20]$ N of the TCAMs, allowing for a static analysis of the arm's deformation under water at each tension level. The

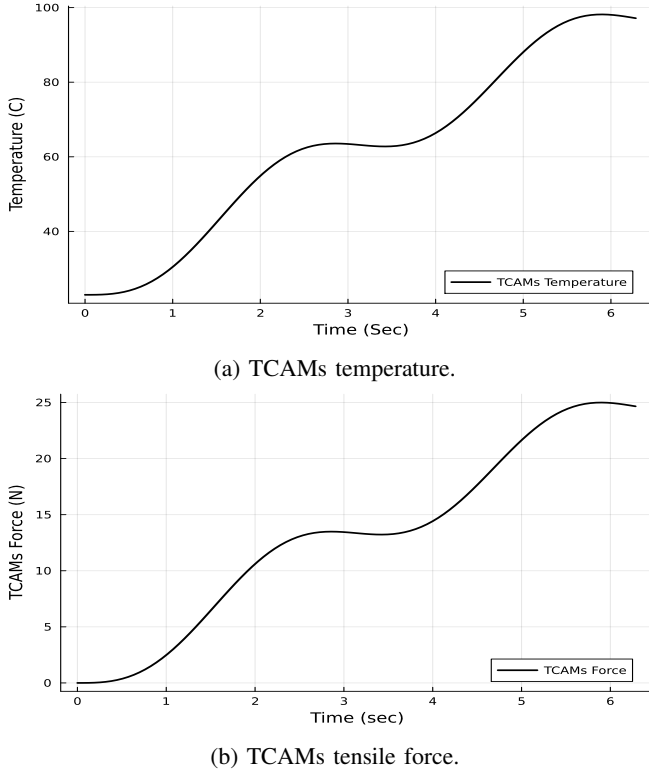


Fig. 2: TCAMs temperature and tensile force, actuated by a sinusoidal voltage.

parameters and dimensions for both case studies are provided in Table II. Fig. 3 illustrates the deformations of the arm for

TABLE II: Parameters of silicone rubber and water.

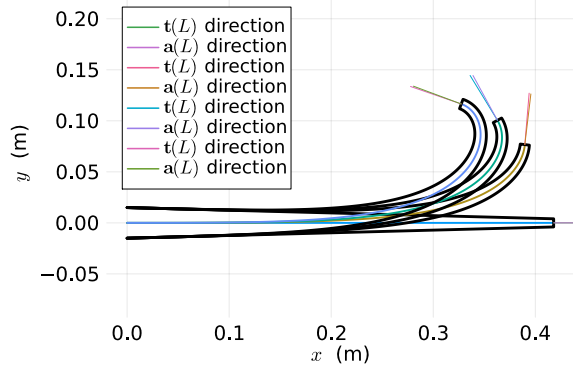
Parameters	Values
E	10 MPa
ν_p	0.5
ρ	1.1 Kg/dm ³
g^r	9.81 m/s ²
R_{min}	4 mm
R_{max}	15 mm
L	418 mm
a_1	12 mm
b_1	1 mm
ρ_w	0.998 Kg/dm ³
μ_v	1.002 mPa.s
v_∞	0.2, 0.4 m/s
T_{11}	[0, 20] N
T_{12}	0.0 N

various tensions $T_{11} \in [0, 20]$ N applied by the TCAMs and for two water free-stream velocities, $v_\infty = 0.2$ m/s and 0.4 m/s. The direction of the tangent vector $\mathbf{t}(L)$ in (2) to the centerline of the arm at $s = L$, and the direction of the unit director $\mathbf{a}(L)$ at $s = L$, are displayed on each configuration of the rod in both Fig. 3a and 3b. It is notable that traditional rod theories do not account for any deformation or rigid rotation of the cross section. Consequently, the cross section at any

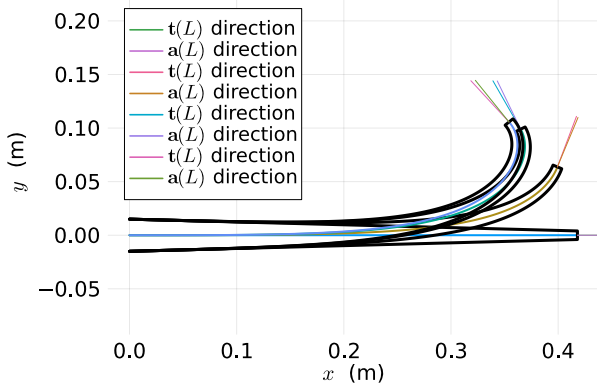
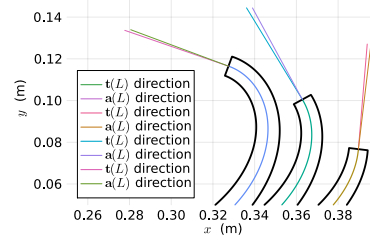
$s \in [0, L]$ always remains perpendicular to the tangent line of the centerline. In other words, the tangent vector $\mathbf{t}(L)$ in Fig. 3 signifies the orientation of the cross section of the rod at $s = L$, before any rigid rotation. On the other hand, in the standard Cosserat theory of rods, the unit director $\mathbf{a}(s)$ is defined such that it always remains perpendicular to the cross section of the rod through deformation and signifies the orientation of the cross section after rigid rotation. Therefore, each unit director $\mathbf{a}(L)$ in Fig. 3 shows the orientation of the rotated cross section at $s = L$ for the corresponding configuration.

Fig. 3 demonstrates that as the tension of the TCAMs $T_{11} \in [0, 20]$ increases, the overall deformation of the arm gradually amplifies. This is observed in both scenarios of water free-stream velocities: $v_\infty = 0.2$ m/s (Fig. 3a) and $v_\infty = 0.4$ m/s (Fig. 3b). Specifically, at $s = L$, the tip of the arm reaches heights of $y = 11.65$ cm and 10.56 cm respectively for these velocities under the constant tension $T_{11} = 20$ N. This implies that for the same tension T_{11} , the overall deformation of the arm, measured by the height of its tip at $s = L$, is less pronounced at higher water free-stream velocities. This reduction in bulk deformation is primarily attributed to the effects of drag force and the dynamic forces exerted by the water flow on the arm's surface, where both the drag force and resulting dynamic force are proportional to the square of the flow velocity. The dynamic force in a steady-state flow results from changes in linear momentum (velocity vector) within the fluid's control volume between two open surfaces. This alteration in momentum does not solely stem from friction between the arm's surface and the water, as it can occur even in the flow of an inviscid fluid over a frictionless body surface. Fig. 3c visually compares the bulk deformation of arm configurations under the constant tension of TCAMs $T_{11} = 20$ N for two scenarios: water free-stream velocities $v_\infty = 0.2$ m/s and $v_\infty = 0.4$ m/s. This comparison underscores that, when subjected to the same tension T_{11} , the arm experiences less deformation at higher free-stream flow velocities.

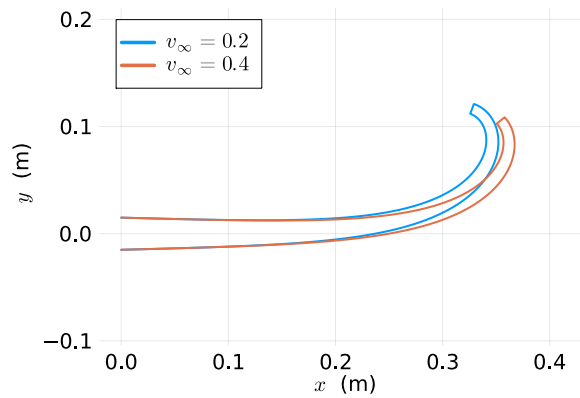
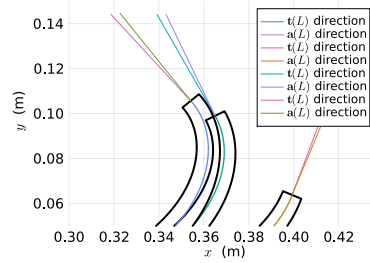
Fig. 4a illustrates the variation of the *tilt angle*, $(\alpha - \theta)(s) \in [0, 180]$, of the rod's cross section at $s = L$ (see Fig. 1b) across tensions of TCAMs $T_{11} \in [0, 20]$ N, for water free-stream velocities $v_\infty = 0.2$ and $v_\infty = 0.4$ m/s. From Fig. 1b, $\alpha(s) \in \mathbb{R}$ and $\theta(s) \in \mathbb{R}$ respectively signify the orientations of the cross section before and after the rigid rotation of the cross section. In essence, $(\alpha - \theta)^\circ(L)$ depicted in Figure 4a indicates how much the cross section deviates from its original perpendicular orientation due to the rod's deformation. Figure 4a demonstrates that in the straight arm, the tangent vector $\mathbf{t}(L)$ aligns with the unit director $\mathbf{a}(L)$ (see Figs. 3a and 3b) for both water free-stream velocities. Figure 4a illustrates that $(\alpha - \theta)^\circ(L)$ is consistently positive for both $v_\infty = 0.2$ and $v_\infty = 0.4$ m/s across all TCAMs tensions $T_{11} \in [0, 20]$ N. This implies $\alpha(L) \geq \theta(L)$ algebraically, indicating a clockwise tilt of the rod's cross section at every tension and for both water velocities. The clockwise rotation is visually confirmed by the orientations of $\mathbf{t}(L)$ and $\mathbf{a}(L)$ in Figs. 3a and 3b. The orientation of the cross section at $s = L$ is influenced by two primary factors: 1) the difference in curvatures between the ventral and dorsal surfaces of the



(a) Deformations for some $T_{11} \in [0, 20]$ and $v_\infty = 0.2$ m/s.



(b) Deformations for some $T_{11} \in [0, 20]$ and $v_\infty = 0.4$ m/s.



(c) Deformations for $T_{11} = 20$ N and $v_\infty = 0.2, 0.4$ m/s.

Fig. 3: Deformations for various tensions of TCAMs $T_{11} \in [0, 20]$ N and water free-stream velocities $v_\infty = 0.2, 0.4$ m/s.

rod, and 2) the concentrated force exerted by the TCAMs $\mathbf{f}_{ij}^{cc}(L)$ as defined in (17). For TCAM tensions $T_{11} \in [0, 20]$ N and $T_{12} = 0$ N, which produce counterclockwise bent configurations as seen in Figs. 3a and 3b, the curvature of the ventral surface at any point $s \in [0, L]$ is generally greater than or equal to the curvature of the dorsal surface at the same point $s \in [0, L]$. The cumulative effect of these local curvature differences along the ventral and dorsal surfaces drives the clockwise rotation of the cross section at $s = L$, as depicted in Fig. 3. The initial increase in the tilt angle $(\alpha - \theta)^\circ(L)$ shown in Fig. 4a is attributed to the heightened curvatures of the ventral and dorsal surfaces of the arm for higher TCAM tensions. This results in increasing differences in local curvatures, consequently leading to a larger tilt angle $(\alpha - \theta)^\circ(L)$ at $s = L$. Conversely, the decreasing trend of the tilt angle, observed at $T_{11} \in [13, 20]$ N for $v_\infty = 0.2$ m/s and at $T_{11} \in [17.5, 20]$ N for $v_\infty = 0.4$ m/s, is driven by the increasing concentrated force of the TCAMs $\mathbf{f}_{ij}^{cc}(L)$. This concentrated force induces a counterclockwise rotation in the cross section at $s = L$, opposing the clockwise rotation caused by the curvature differences along the ventral and dorsal surfaces. Fig. 4a illustrates that the tilt angle reaches larger values for a water free-stream velocity of $v_\infty = 0.4$ m/s compared to $v_\infty = 0.2$ m/s, under the same tensions $T_{11} \in [9, 20]$. This accelerated increase in tilt angle can be attributed to the faster growth of angle $\theta^\circ \in [0, 180]$ observed at $v_\infty = 0.2$ m/s, as shown in Figure 4b. Fig. 4c displays the variation of the tilt angle along the arm for selected tensions $T_{11} \in [0, 20]$ N and at $v_\infty = 0.2$ m/s. The positive tilt angle implies clockwise rotation of the cross section along the arm. Note that, the downward trend near the rod's end is influenced by the increasing concentrated force of TCAMs at higher tensions.

The variation of the cross-sectional normal strain $\beta(s) \in \mathbb{R}$ along the arm is depicted in Figure 4d for various tensions $T_{11} \in [0, 20]$ N under a water free-stream velocity of $v_\infty = 0.2$ m/s. $\beta(s)$ represents the planar deformation of the cross-section in the direction of the standard unit director $\mathbf{b}(s) \in \mathbb{R}^2$. This deformation enables the arm's cross-section to adjust locally while preserving the local volume. This behavior aligns with the biomechanical principles observed in octopus arms, where tissue stiffness depends on incompressibility. Fig. 4d indicates that $\beta(s)$ increases monotonically along the arm for all tensions $T_{11} \in [0, 20]$. To further explore arm mechanics, Fig. 5 illustrates the variations in the normal $N(s)$ and shear $H(s)$ tractions, as well as the bending moment $M(s)$ along the arm for selected TCAM tensions.

2) *Validation*: To validate the Cosserat-based model for the octopus-like arm in water, Ansys simulations were conducted under similar conditions. Due to the limitations of beam elements in Ansys for fluid-structure interaction (FSI) analysis, three-dimensional (3D) solid elements were utilized, and an FSI approach was employed to accurately model the interaction between the soft arm and the steady-state water flow. Fig. 6 shows the deformations of the arm modeled in Ansys with FSI, while Figs. 7 and 8 respectively present the distribution of velocity and pressure fields over the arm.

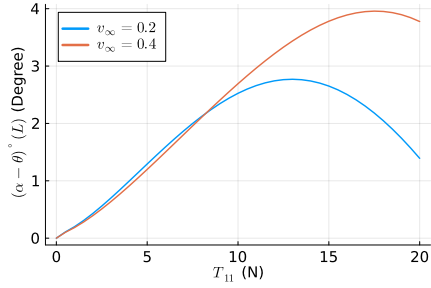
The Ansys simulation results generally show strong agreement with the Cosserat-based model, particularly in terms of the maximum deformations at the arm tip, confirming the model's accuracy. However, some discrepancies are observed at the arm tip, where the Ansys results differ in curvature compared to the Cosserat-based results. This divergence arises because the extended Cosserat theory models the arm as a rod, effectively capturing the complex behavior of the arm's curvature and the orientation of its cross-section, which are particularly critical at the tip where curvature is more pronounced. In contrast, the 3D solid elements in Ansys do not explicitly model the arm's curvature as a rod or the orientation of the cross-section, leading to variations in predicted curvature and overall deformation, especially in regions with higher curvature. This difference in modeling approaches explains the observed discrepancies, particularly at the arm's tip.

IX. CONCLUSIONS

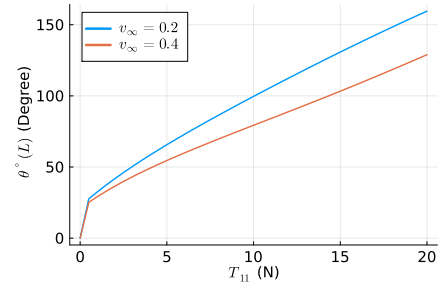
This study explored the use of recently developed TCAMs to actuate and replicate the bending motion of an octopus-like soft robot arm underwater. A quasi-static continuum model was developed to examine the effects of hydrostatic and dynamic forces from steady-state fluid flow on the arm's bending motion. The extended Cosserat theory of rods was used to model the soft robot arm as a continuum robot, allowing for rigid rotation of the cross-section without constraining it to be locally normal to the rod's direction. Unlike the standard Cosserat theory, this approach included planar deformation of the cross-section, introducing a new normal strain to describe in-plane deformation. A constitutive model for the octopus arm material was also proposed to capture its characteristic behavior.

REFERENCES

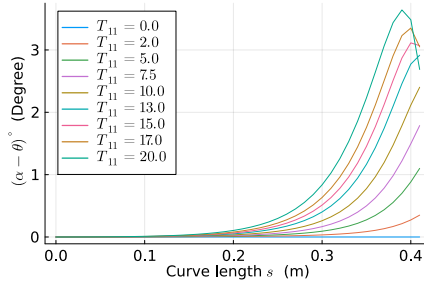
- [1] Stuart S. Antman. *Nonlinear Problems of Elasticity*. Springer, 2005.
- [2] Costanza Armanini, Frédéric Boyer, Anup Teejo Mathew, Christian Duriez, and Federico Renda. Soft robots modeling: A structured overview. *IEEE Transactions on Robotics*, 39(3):1728–1748, 2023.
- [3] Frederic Boyer, Vincent Lebastard, Fabien Candelier, and Federico Renda. Dynamics of continuum and soft robots: A strain parameterization based approach. *IEEE Transactions on Robotics*, 37(3):847–863, 2021.
- [4] David B. Camarillo, Christopher F. Milne, Christopher R. Carlson, Michael R. Zinn, and J. Kenneth Salisbury. Mechanics modeling of tendon-driven continuum manipulators. *IEEE Transactions on Robotics*, 24(6):1262–1273, 2008.
- [5] Gregory S. Chirikjian. *Theory and Applications of Hyper-Redundant Robotic Manipulators*. PhD thesis, California Institute of Technology, 1992.
- [6] Gregory S. Chirikjian and J.W. Burdick. Kinematically optimal hyper-redundant manipulator configurations. *IEEE TRANSACTIONS ON ROBOTICS AND AUTOMATION*, 11(6):794–806, 1995.
- [7] G.S. Chirikjian and J.W. Burdick. A modal approach to hyper-redundant manipulator kinematics. *IEEE Transactions on Robotics and Automation*, 10(3):343–354, 1994.
- [8] Cosimo Della Santina, Robert K. Katzschmann, Antonio Biechi, and Daniela Rus. Dynamic control of soft robots interacting with the environment. In *2018 IEEE International Conference on Soft Robotics (RoboSoft)*, pages 46–53, 2018.
- [9] Azadeh Doroudchi and Spring Berman. Configuration tracking for soft continuum robotic arms using inverse dynamic control of a cosserat rod model. In *2021 IEEE 4th International Conference on Soft Robotics (RoboSoft)*, pages 207–214, 2021.



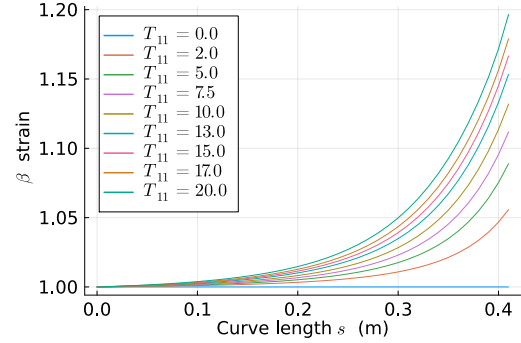
(a) Tilt angle $(\alpha - \theta)^\circ \in [0, 180]$ at $s = L$.



(b) Angle $\theta^\circ \in [0, 180]$ at $s = L$.



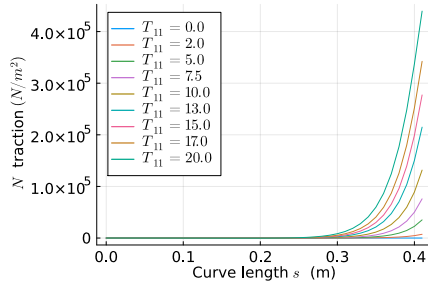
(c) Tilt angle $(\alpha - \theta)^\circ \in [0, 180]$ along the rod for $v_\infty = 0.2$ m/s.



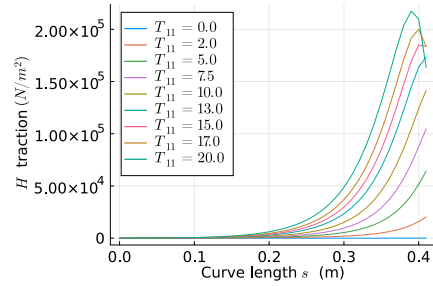
(d) Normal strain $\beta(s)$ along the rod for $v_\infty = 0.2$ m/s.

Fig. 4: Variations of angles $(\alpha - \theta)^\circ$, θ° , and cross-sectional strain $\beta(s)$.

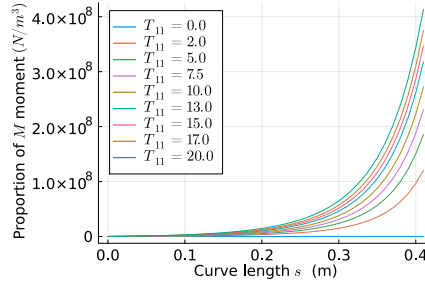
- [10] Michele Giorelli, Federico Renda, Marcello Calisti, Andrea Arienti, Gabriele Ferri, and Cecilia Laschi. A two dimensional inverse kinetics model of a cable driven manipulator inspired by the octopus arm. In *2012 IEEE International Conference on Robotics and Automation*, pages 3819–3824, 2012.
- [11] Valentina Giovinco, Parth Kotak, Venanzio Cichella, Carmine Maletta, and Caterina Lamuta. Dynamic model for the tensile actuation of thermally and electro-thermally actuated twisted and coiled artificial muscles (tcams). *Smart Materials and Structures*, 29(2):025004, dec 2019.
- [12] Gianpaolo Gulletta, Wolfram Erhagen, and Estela Bicho. Human-like arm motion generation: A review. *Robotics*, 9(4), 2020.
- [13] Carter S. Haines, Márcio D. Lima, Na Li, Geoffrey M. Spinks, Javad Foroughi, John D. W. Madden, Shi Hyeong Kim, Shaoli Fang, Mônica Jung de Andrade, Fatma Göktepe, Özer Göktepe, Seyed M. Mirvakili, Sina Naficy, Xavier Lepró, Jiyoung Oh, Mikhail E. Kozlov, Seon Jeong Kim, Xiuru Xu, Benjamin J. Swedlove, Gordon G. Wallace, and Ray H. Baughman. Artificial muscles from fishing line and sewing thread. *Science*, 343(6173):868–872, 2014.
- [14] Maxwell Hammond, Venanzio Cichella, Thilina Weerakkody, and Caterina Lamuta. Robust and adaptive sampled-data control of twisted and coiled artificial muscles. *IEEE Control Systems Letters*, 6:1232–1237, 2022.
- [15] Michael W. Hannan and Ian D. Walker. Kinematics and the implementation of an elephant’s trunk manipulator and other continuum style robots. *Journal of Robotic Systems*, 20(2):45–63, 2003.
- [16] Akira Kato, Masato Hirabayashi, Yuya Matsumoto, Yasutaka Nakashima, Yo Kobayashi, Masakatsu G. Fujie, and Shigeki Sugano. Continuous wrist joint control using muscle deformation measured on forearm skin. In *2018 IEEE International Conference on Robotics and Automation (ICRA)*, pages 1818–1824. IEEE Press, 2018.
- [17] Robert K. Katzschmann, Cosimo Della Santina, Yasunori Toshimitsu, Antonio Bicchi, and Daniela Rus. Dynamic motion control of multi-segment soft robots using piecewise constant curvature matched with an augmented rigid body model. In *2019 2nd IEEE International Conference on Soft Robotics (RoboSoft)*, pages 454–461, 2019.
- [18] Parth Kotak, Jason M Wilken, Kirsten M Anderson, and Caterina Lamuta. Carbon fiber-based twisted and coiled artificial muscles (tcams) for powered ankle-foot orthoses. *J Biomech Eng*, 144(1), Jan 2022.
- [19] Ajeet Kumar and Subrata Mukherjee. A Geometrically Exact Rod Model Including In-Plane Cross-Sectional Deformation. *Journal of Applied Mechanics*, 78(1), 10 2010. 011010.
- [20] C Lamuta, S Messelot, and S Tawfik. Theory of the tensile actuation of fiber reinforced coiled muscles. *Smart Materials and Structures*, 27(5):055018, apr 2018.
- [21] C Laschi, B Mazzolai, V Mattoli, M Cianchetti, and P Dario. Design of a biomimetic robotic octopus arm. *Bioinspir Biomim*, 4(1):015006, Mar 2009.
- [22] Xueqi Leng, Xiaoyu Hu, Wubin Zhao, Baigang An, Xiang Zhou, and Zunfeng Liu. Recent advances in twisted-fiber artificial muscles. *Advanced Intelligent Systems*, 3(5):2000185, 2021.
- [23] Andrew D. Marchese, Russ Tedrake, and Daniela Rus. Dynamics and trajectory optimization for a soft spatial fluidic elastomer manipulator. In *2015 IEEE International Conference on Robotics and Automation (ICRA)*, pages 2528–2535, 2015.
- [24] Guodong Qin, Aihong Ji, Yong Cheng, Wenlong Zhao, Hongtao Pan, Shanshuang Shi, and Yuntao Song. A snake-inspired layer-driven continuum robot. *Soft Robotics*, 9(4):788–797, 2022. PMID: 34550801.
- [25] Longhui Qin, Haijun Peng, Xiaonan Huang, Mingchao Liu, and Weicheng Huang. Modeling and simulation of dynamics in soft robotics: a review of numerical approaches. *Current Robotics Reports*, 5(1):1–13, 2024.
- [26] Federico Renda, Costanza Armanini, Vincent Lebastard, Fabien Candelier, and Frederic Boyer. A geometric variable-strain approach for static modeling of soft manipulators with tendon and fluidic actuation. *IEEE Robotics and Automation Letters*, 5(3):4006–4013, 2020.
- [27] Federico Renda, Frédéric Boyer, Jorge Dias, and Lakmal Seneviratne. Discrete cosserat approach for multisection soft manipulator dynamics. *IEEE Transactions on Robotics*, 34(6):1518–1533, 2018.
- [28] Federico Renda, Michele Giorelli, Marcello Calisti, Matteo Cianchetti, and Cecilia Laschi. Dynamic model of a multibending soft robot arm driven by cables. *IEEE Transactions on Robotics*, 30(5):1109–1122, 2014.
- [29] Federico Renda and Cecilia Laschi. A general mechanical model for tendon-driven continuum manipulators. In *2012 IEEE International Conference on Robotics and Automation*, pages 3813–3818, 2012.
- [30] III Robert J. Webster and Bryan A. Jones. Design and kinematic modeling of constant curvature continuum robots: A review. *The International Journal of Robotics Research*, 29(13):1661–1683, 2010.



(a) Normal traction $N(s)$ along the rod.

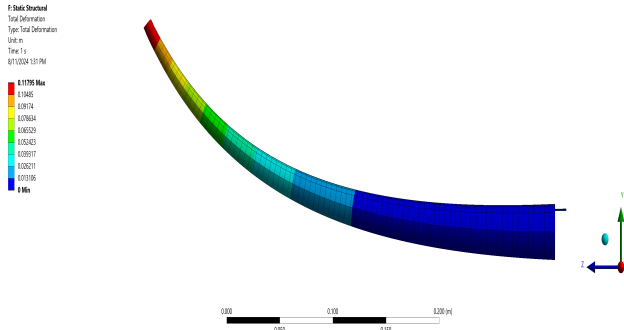


(b) Shear traction $H(s)$ along the rod.

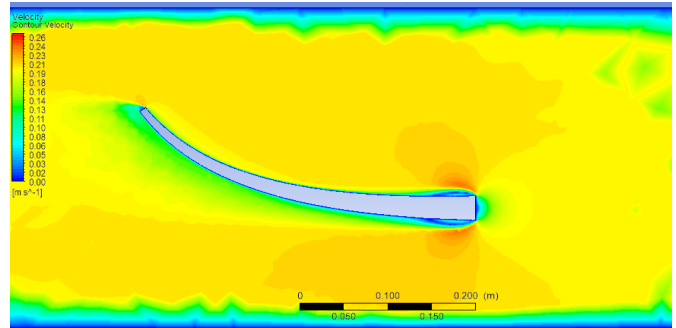


(c) Bending moment $M(s)$ along the rod.

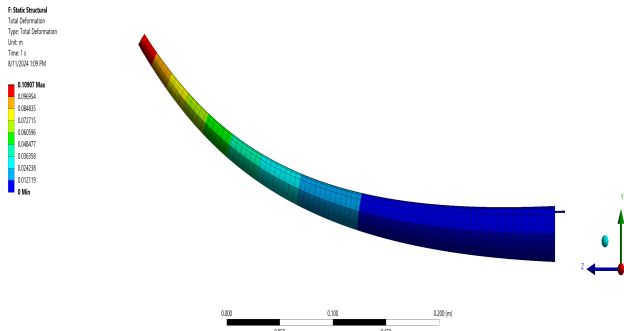
Fig. 5: Normal $N(s)$ and shear $H(s)$ tractions and bending moment $M(s)$ along the rod $s \in [0, L]$ for some tensions of the TCAMs $T_{11} \in [0, 20]$ and water free-stream velocity of $v_\infty = 0.2$ m/s.



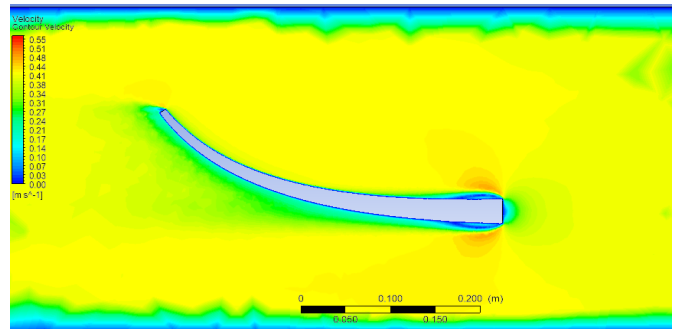
(a) Arm deformation for $v_\infty = 0.2$ m/s.



(a) Velocity field over the arm for $v_\infty = 0.2$ m/s.



(b) Arm deformation for $v_\infty = 0.4$ m/s.



(b) Velocity field over the arm for $v_\infty = 0.4$ m/s.

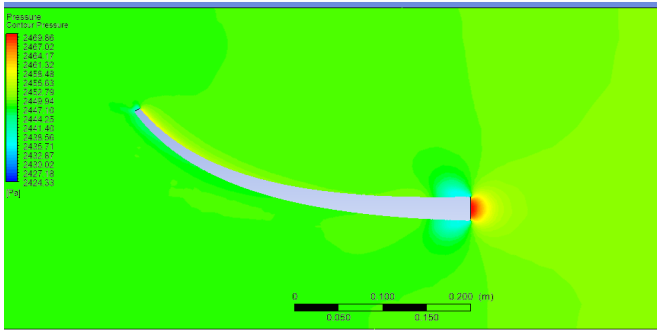
Fig. 6: Deformations of the arm modeled in Ansys with FSI.

Fig. 7: Distribution of the velocity fields over the arm.

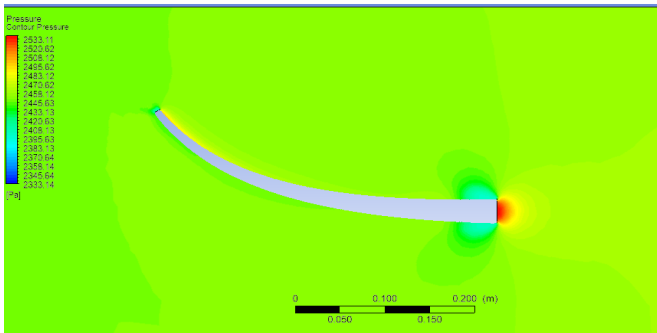
[31] G. Robinson and J.B.C. Davies. Continuum robots - a state of the art. In *Proceedings 1999 IEEE International Conference on Robotics and Automation (Cat. No.99CH36288C)*, volume 4, pages 2849–2854 vol.4, 1999.

[32] Majid Roshanfar, Javad Dargahi, and Amir Hooshair. Cosserat rod-based dynamic modeling of a hybrid-actuated soft robot for robot-assisted cardiac ablation. *Actuators*, 13(1), 2024.

[33] Daniela Rus and Michael T. Tolley. Design, fabrication and control of



(a) Pressure field over the arm for $v_\infty = 0.2 \text{ m/s}$.



(b) Pressure field over the arm for $v_\infty = 0.4 \text{ m/s}$.

Fig. 8: Distribution of the pressure fields over the arm.

soft robots. *Nature*, 521(7553):467–475, 2015.

- [34] Lokesh Saharan and Yonas T. Tadesse. Novel twisted and coiled polymer artificial muscles for biomedical and robotics applications. *Materials for Biomedical Engineering*, 2019.
- [35] Amir Sayadi, Renzo Cecere, and Amir Hooshier. Finite arc method: Fast-solution extended piecewise constant curvature model of soft robots with large variable curvature deformations. *Robotics Reports*, 2(1):49–64, 2024.
- [36] Jiefeng Sun and Jianguo Zhao. Physics-based modeling of twisted-and-coiled actuators using cosserat rod theory. *IEEE Transactions on Robotics*, 38(2):779–796, 2022.
- [37] Enver Tatlicioglu, Ian D. Walker, and Darren M. Dawson. New dynamic models for planar extensible continuum robot manipulators. In *2007 IEEE/RSJ International Conference on Intelligent Robots and Systems*, pages 1485–1490, 2007.
- [38] Sameh Tawfik and Yichao Tang. Stronger artificial muscles, with a twist. *Science*, 365(6449):125–126, 2019.
- [39] John Till, Vincent Aloï, and Caleb Rucker. Real-time dynamics of soft and continuum robots based on cosserat rod models. *The International Journal of Robotics Research*, 38(6):723–746, 2019.
- [40] Deepak Trivedi, Christopher D. Rahn, William M. Kier, and Ian D. Walker. Soft robotics: Biological inspiration, state of the art, and future research. *Applied Bionics and Biomechanics*, 5(3):520417, 2008.
- [41] Thilina H. Weerakkody, Maxwell Hammond, James H. Neilan, Venanzio Cichella, and Caterina Lamuta. Modeling and control of twisted and coiled artificial muscles for soft robotics. *Meccanica*, 58(4):643–658, 2023.
- [42] Lingxiao Xun, Gang Zheng, and Alexandre Kruszewski. Cosserat-rod-based dynamic modeling of soft slender robot interacting with environment. *IEEE TRANSACTIONS ON ROBOTICS*, 40:2811–2830, 2024.
- [43] Sang Yul Yang, Kyeong Ho Cho, Youngeun Kim, Min-Geun Song, Ho Sang Jung, Ji Wang Yoo, Hyungpil Moon, Ja Choon Koo, Jae do Nam, and Hyouk Ryeol Choi. High performance twisted and coiled soft actuator with spandex fiber for artificial muscles. *Smart Materials and Structures*, 26(10):105025, sep 2017.
- [44] Michael C. Yip and Günter Niemeyer. High-performance robotic muscles from conductive nylon sewing thread. In *2015 IEEE International*